

Effect of spin-dependent tunneling in a $\text{MoSe}_2/\text{Cr}_2\text{Ge}_2\text{Te}_6$ van der Waals heterostructure on exciton and trion emission

Annika Bergmann,¹ Swarup Deb,¹ Veronika Schneidt,¹ Mustafa Hemaïd,¹
Kenji Watanabe,² Takashi Taniguchi,³ Rico Schwartz,¹ and Tobias Korn^{1,*}

¹*Institute of Physics, Rostock University, 18059 Rostock, Germany*

²*Research Center for Electronic and Optical Materials, NIMS, 1-1 Namiki, Tsukuba 305-0044, Japan*

³*Research Center for Materials Nanoarchitectonics, NIMS, 1-1 Namiki, Tsukuba 305-0044, Japan*

We study van der Waals heterostructures consisting of monolayer MoSe_2 and few-layer $\text{Cr}_2\text{Ge}_2\text{Te}_6$ fully encapsulated in hexagonal Boron Nitride using low-temperature photoluminescence and polar magneto-optic Kerr effect measurements. Photoluminescence characterization reveals a partial quenching and a change of the exciton-trion emission ratio in the heterostructure as compared to the isolated MoSe_2 monolayer. Under circularly polarized excitation, we find that the exciton-trion emission ratio depends on the relative orientation of excitation helicity and $\text{Cr}_2\text{Ge}_2\text{Te}_6$ magnetization, even though the photoluminescence emission itself is unpolarized. This observation hints at an ultrafast, spin-dependent interlayer charge transfer that competes with exciton and trion formation and recombination.

I. INTRODUCTION

In recent years, two-dimensional (2D) crystals and van der Waals (vdW) heterostructures [1] consisting of different 2D materials have been one of the most active fields in solid-state research. Besides graphene, the semiconducting transition metal dichalcogenides (TMDCs) such as MoSe_2 have garnered a lot of research attention. This is due to their exciting electronic and optical properties. In the monolayer (ML) limit, they become direct-gap semiconductors [2] with a peculiar band structure leading to spin-valley coupling [3]. These properties make them potentially interesting for spintronics [4] and valleytronics [5], where information is encoded in the spin or valley degree of freedom of carriers, instead of their charge. In ML TMDCs, the optical selection rules allow generation of a coupled spin-valley polarization of excitons using circularly polarized excitation, and the excitonic valley polarization degree can be read out directly in helicity-resolved photoluminescence (PL) measurements [6, 7]. Depending on the specific TMDC material, this mechanism for generating a valley polarization can be very effective and robust, even for highly nonresonant excitation.

For the specific case of MoSe_2 , however, the valley relaxation rate is extremely fast compared to that of exciton recombination, so that a significant circular polarization of the PL emission can only be observed for near-resonant excitation [8–10]. Despite the unfavorable relaxation rates, an excitonic valley polarization can be achieved by lifting the energy degeneracy of opposite valleys. A usual strategy has been to exploit external magnetic fields perpendicular to the plane of a TMDC ML to break time-reversal symmetry. This introduces a valley Zeeman splitting and leads to a preferential occupation of the energetically favorable valley, even for unpolarized and

nonresonant excitation [11, 12]. However, the effective g factors for TMDC monolayers correspond to a splitting of only about 0.2 meV per Tesla, so that magnetic fields of several Tesla are required to achieve a significant valley polarisation even at liquid helium temperature.

As such field strengths are impractical for device applications, the use of magnetic proximity effects [13], where the proximity of a magnetic material induces a magnetization through exchange interaction, has been explored in recent years. This has made it possible to tailor the spin-valley properties in TMDCs without the need for an external magnetic field [14]. Alternatively, spin injection from ferromagnetic materials was used to generate valley polarization in TMDCs [15]. A variety of bulk ferromagnetic materials ranging from metals like Nickel [16] to ferromagnetic semiconductors such as $\text{Ga}(\text{Mn})\text{As}$ [15] and EuS [17] were employed in experimental studies. However, the presence of surface states, dangling bonds, interface reconstruction etc. greatly complicates their integration into vdW heterostructures.

For this, layered ferromagnetic materials [18, 19], made of chemically stable atomically thin sheets, have recently emerged as a viable alternative for integration into vdW heterostructures. While there have been a number of experimental studies [14, 20–22], among the plethora of available TMDC and vdW ferromagnets, it remains elusive which material combinations, thicknesses, and other parameters offer the best material platform for studying phenomena such as spin-dependent tunneling and magnetic proximity effects.

Here, we report on an optical spectroscopy study of vdW heterostructures consisting of monolayer MoSe_2 and the ferromagnetic semiconductor $\text{Cr}_2\text{Ge}_2\text{Te}_6$ (CGT) [23, 24] encapsulated in hexagonal Boron Nitride (hBN). Low-temperature photoluminescence measurements reveal a partial quenching of the PL and a significantly reduced trion-to-exciton emission ratio in the heterostructure as compared to an isolated MoSe_2 ML, indicating an electron transfer from the MoSe_2 into the CGT. Under nonres-

* tobias.korn@uni-rostock.de

onant, circularly polarized excitation, we find that the exciton-trion ratio depends on the relative orientation of excitation helicity and CGT magnetization. Remarkably, this effect is observable even though the PL emission itself is unpolarized, indicating a vanishing valley polarization of excitons and trions. We interpret these observations as an interplay of spin-dependent tunneling of the initially valley-polarized electrons from MoSe₂ into CGT with exciton and trion formation, valley relaxation and recombination.

Our findings offer a glimpse into material combinations that can be utilized for spin generation and hosting, and more importantly, provide a potential means to read out spin polarization through spin-selective tunneling - an essential component in the process and measurement chain of spin-valleytronic devices.

II. RESULTS AND DISCUSSION

To begin with, we discuss the structure and characterization of our samples. As an example, Figure 1a shows a fully hBN-encapsulated MoSe₂/CGT heterostructure. Attached to bulk CGT, two thin CGT regions I and II of different thickness cover an underlying MoSe₂ monolayer and are thus of particular interest. After exfoliation, optical images of the CGT flake were taken in transmission mode inside an inert gas glovebox used for sample preparation (see methods). From the absorbance in conjunction with AFM measurements, we estimate the CGT flake to consist of 14 layers in region I and of 9 layers in region II (see supplementary information Figure S1). Low-temperature PL measurements at 5 K were used to characterize the resulting heterostructure. The PL map of the sample depicted in Figure 1b reveals a quenching by a factor of five of the MoSe₂ monolayer emission in the heterostructure region compared to the isolated MoSe₂ monolayer, indicating a high-quality interfacial contact for interlayer charge transfer between both layers [25]. Whereas the isolated monolayer spectrum is dominated by trion emission, the trion-exciton ratio is significantly smaller in the heterostructure region (Figure 1c). Whether either trion or exciton emission is more pronounced in the spectrum depends on the position on the heterostructure, which we attribute to locally different interface qualities due to inclusions between the two layers.

For further polarization-resolved PL measurements, a fully saturated magnetization along the out-of-plane axis of the CGT flake is crucial. This makes the magnetization (anti-)parallel to the spin orientation in the TMDC *K* valleys. Polar magneto-optical Kerr effect (MOKE) measurements at a nominal sample temperature of 5 K (illustrated in Figure 1d) show a hysteresis loop with small remanence and low coercive field for region II. By contrast, we find a more complex, bow-tie-like shape of the hysteresis loop for the thicker region I, which resembles previous reports on hysteresis loops for CGT flakes thicker than 13 layers [26] or 10 nm [27], closely matching our thick-

ness estimates based on absorbance. As a consequence of the small magnetic remanence observed in MOKE, all subsequent measurements were conducted at an external magnetic field of ± 50 mT, ensuring magnetization saturation parallel to the direction of the external magnetic field.

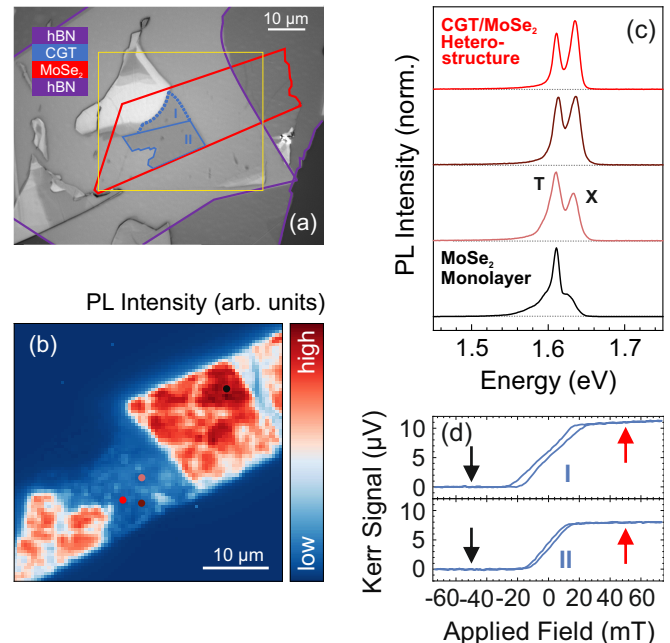


Figure 1. (a) Optical microscope image of an hBN-encapsulated MoSe₂/CGT heterostructure. A CGT flake with regions of various layer thickness (I and II) covers an underlying MoSe₂ monolayer. The yellow box corresponds to the false colour map of the PL scan area (b), showing quenching of the MoSe₂ monolayer emission in the heterostructure region. (c) Compared to the MoSe₂ monolayer, the ratio of trion (T) and exciton (X) is reduced in the heterostructure, with different exciton-trion ratios observed, depending on the measurement position. All spectra were taken from the PL scan. Their positions are marked by the coloured dots corresponding to the colour of the spectrum. (d) MOKE measurements prove ferromagnetic behaviour of the CGT flake. Magnetic saturation is reached at 32 mT and 18 mT for I and II, respectively. The arrows indicate the applied field of ± 50 mT for the helicity-resolved measurements described below.

Valley polarization effects were investigated by nonresonant PL measurements using an excitation wavelength of 633 nm. Circularly polarized excitation was achieved using an achromatic quarter-wave-plate ($\lambda/4$ -plate). A second $\lambda/4$ -plate in conjunction with a linear polarizer was used for helicity-resolved detection. With a constant excitation helicity, multiple PL spectra were measured with alternating magnetic field direction. Spectra recorded at the same magnetic field direction were then summed up to improve the signal-to-noise ratio. This was repeated for the opposite excitation helicity. We emphasize that in these measurements the detection helicity was fixed. Remarkably, the population dynamics described below is observed irrespective the detection helicity and can

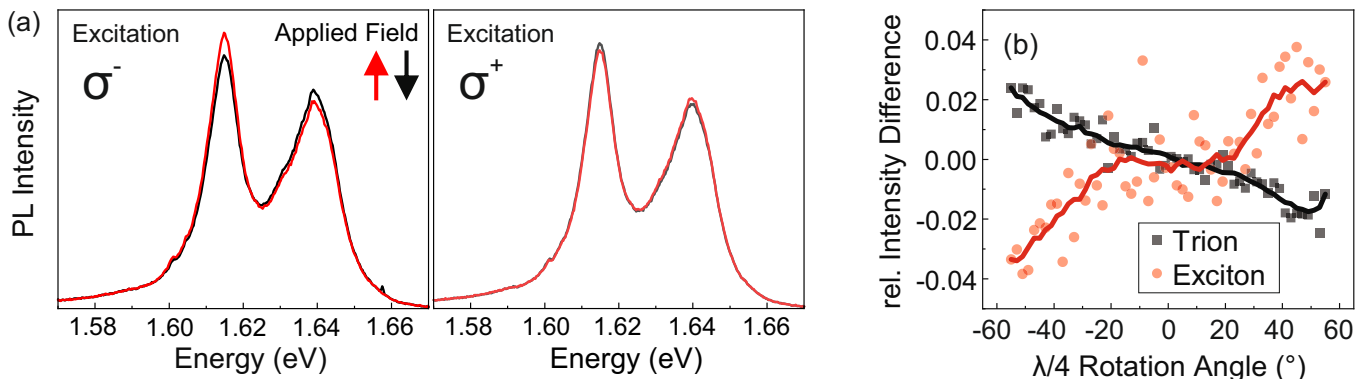


Figure 2. (a) Low-temperature PL spectra taken in the heterostructure region in presence of an external magnetic field for left (σ^-) and right (σ^+) circularly polarized excitation. For a fixed excitation helicity, trion and exciton intensities change in dependence of the magnetic field direction (arrows). (b) The relative intensity difference for exciton and trion upon flip of magnetic field depends on the degree of circularly polarized excitation, vanishing for linear polarization at a $\lambda/4$ rotation angle close to 0° . The solid lines represent the sliding average of eight data points and serve as guide to the eye.

also be seen in linearly polarized detection (Figure S2). Figure 2a shows evidence for magnetic-field-dependent changes of exciton and trion emission. For left-polarized (σ^-) excitation populating the K^- valley, the trion intensity is larger when a positive (red) magnetic field is applied, compared to a negative (black) magnetic field of the same magnitude. The opposite trend is observed for exciton emission where a larger intensity is observed in a negative magnetic field. In contrast, under right-polarized (σ^+) excitation the intensity distributions for both trion and exciton are reversed. However, the magnetic-field-dependent intensity variation has a different magnitude for right and left circularly polarized excitation. We attribute this to a minor deviation from the optimum excitation helicity. In addition, a small beam offset induced by rotating the $\lambda/4$ -plate can result in a slightly different excitation spot on the sample. To quantify the magnetic-field-induced intensity differences, we define them as:

$$\Delta I = \frac{I(B \downarrow) - I(B \uparrow)}{I(B \downarrow) + I(B \uparrow)} \quad (1)$$

where $\downarrow\uparrow$ denotes the external magnetic field direction. Changing the degree of circular polarization by rotating the $\lambda/4$ -plate in the excitation (Figure 2b), demonstrates a vanishing intensity difference for linear excitation corresponding to an angle of about 0° , whereas an increasing difference occurs for excitation deviating from linear polarization, reaching maximum values of about 4%.

To confirm that the intensity differences result from an interaction between the MoSe₂ monolayer and the magnetized CGT, the same measurement was performed on an isolated part of the monolayer. Here, the same trion (exciton) intensity was detected irrespective of the magnetic field direction for both left and right circularly polarized excitation (Figure S3).

Based on work functions for both MoSe₂ monolayer and CGT flakes of the determined thickness [21], the heterostructure should possess a type I band alignment with

the MoSe₂ conduction band being energetically higher than that of CGT.

PL quenching of the MoSe₂ emission in the heterostructure region compared to the isolated monolayer as well as the smaller trion-to-exciton ratio in the heterostructure indicates electron transfer from the MoSe₂ into the CGT. We note that there are two mechanisms that can change the exciton-trion ratio in the heterostructure. On one hand, an electron transfer can reduce the background carrier density in MoSe₂, reducing the probability of trion formation. On the other hand, trions in MoSe₂ have significantly longer photoluminescence lifetimes than excitons [8, 28], so that they are more susceptible to non-radiative decay channels, such as electron tunneling into the CGT, during their lifetime.

When analyzing the helicity-dependent changes of exciton and trion emission shown in Figure 2, various processes that occur, both, within the individual layers and in their interaction have to be considered. We first examine the behaviour for right circularly polarized excitation (σ^+), populating the K^+ valley, as it is illustrated in Figure 3. Due to the external magnetic field, the CGT flake is magnetically saturated with the spin states aligned with the external magnetic field direction. In the case of a positive magnetic field, the electrons residing in the K^+ valley therefore have a high density of spin-up states available in the CGT conduction band. This increases the tunneling rate, which reduces the density of electrons in MoSe₂. Thus, less electrons are available for trion formation. In contrast, if a negative magnetic field is applied, the tunneling channel is decreased as a result of the smaller density of states available in the CGT conduction band, and more trions are formed at the expense of excitons. The shifted balance between exciton and trion populations gives rise to an intensity reversal within the spectra upon change of magnetic field direction. Changing the excitation helicity to σ^- inverts the spin-compatibilities with the CGT majority spin states and thus reverses the

behaviour explained above. At this point, it shall again be highlighted that the overall detected PL emission is unpolarized. We ascribe this to intervalley scattering mediated by long-range Coulomb interaction [29] which was identified to be the main mechanism for exciton valley depolarization after initial circular excitation in MoSe₂ [9]. We assume that a considerable fraction of excitons and trions is scattered between the K^+ and K^- valley before exciton and trion recombination take place. The dependence of the intensity difference on the degree of excitation polarization can directly be explained by the different initial populations of the valleys. The imbalance between the two valleys rises as the degree of excitation polarization increases, which is reflected in larger intensity differences upon reversal of the magnetic field. Remarkably, the changes in exciton and trion populations observed in PL are thus a consequence of a spin-dependent tunneling process, even though any initial spin and valley polarization is lost well before exciton and trion recombination.

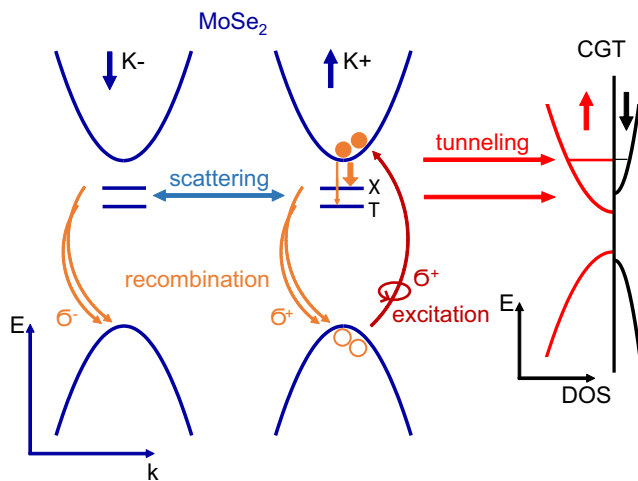


Figure 3. Illustration of processes causing the population dynamics for σ^+ excitation and $B \uparrow$. Spin-up electrons in the K^+ valley tunnel into the CGT due to a high density of spin-up states in the conduction band. The decreased charge carrier density in MoSe₂ reduces the trion formation rate compared to excitons. A change of magnetic field direction would result in a smaller density of spin-up states in the CGT, leading to increased trion formation at the expense of excitons. The initial valley polarization is lost due to scattering between the valleys, causing the collected PL to stem from both valleys. The collected PL is thus irrespective of the detection helicity.

In summary, we have fabricated MoSe₂/CGT heterostructures that reveal charge transfer from the MoSe₂ monolayer into the CGT. The magnetization of the CGT flake enables spin-dependent tunneling after nonresonant, circularly polarized excitation which manifests itself in altered exciton and trion intensities upon change of the external magnetic field direction. Intervalley scattering causes a loss of initial spin and valley polarization prior

to exciton and trion recombination, resulting in an unpolarized collected PL. Our results underline the complex interplay of these competing processes on sub-picosecond timescales.

Given that nonresonant, circularly polarized excitation of our structures yields an exciton/trion occupation imbalance, which is more robust than a valley polarization in MoSe₂, our study paves the way for detection of light helicity without the use of polarization optics.

III. METHODS

A. Sample fabrication

Under ambient conditions, hBN flakes and MoSe₂ monolayers were isolated from bulk crystals by mechanical exfoliation. The hBN flake was stamped with PDMS onto a Si/SiO₂ substrate via deterministic transfer [30]. A MoSe₂ monolayer was deposited on the hBN accordingly and afterwards annealed in mild vacuum. CGT flakes were exfoliated from a bulk crystal (hq Graphene) under nitrogen atmosphere in a glovebox [31], thin flakes were thereby identified under an optical microscope based on their optical contrast. Immediately after exfoliation, the CGT flake was placed on top of the beforehand prepared hBN/MoSe₂ structure using a second deterministic stamping setup and PDMS transfer inside the glovebox. To protect the CGT from oxidation, the heterostructure was then fully encapsulated inside the glovebox by adding an hBN top layer.

B. Optical measurements

1. Photoluminescence

For the PL measurements the sample was excited with a 1.96 eV continuous-wave diode laser focused to a spot size of about 1 μm using an 80x microscope objective. The sample was mounted in a He-flow cryostat and cooled to a nominal temperature of about 5 K. The PL light emitted by the sample is collected using the same objective, filtered by a long pass and analyzed with a combination of a spectrometer and a charge-coupled-device. To obtain PL maps of the sample, the cryostat, with the sample inside, was moved in relation to the fixed laser spot through a computer-controlled xy stage. For helicity-resolved excitation, a linear polarizer and an achromatic quarter-wave plate were placed in the excitation beam path. The wave plate was mounted in a motorized rotation stage, so that its angle could be varied automatically. Similarly, for helicity-resolved detection, an achromatic $\lambda/4$ -plate and a linear polarizer (acting as an analyzer) were placed in the detection beam path in front of the spectrometer. For application of an external magnetic field, an air coil was placed around the cryostat, so that a magnetic field of up to 200 mT could be applied perpendicular to the

sample plane. The current for the coil was supplied by a bipolar current source.

2. Polar magneto-optical Kerr effect

The polar MOKE measurements were performed in the setup described above using the 1.96 eV diode laser. Its intensity was modulated using a flywheel chopper. A beamsplitter cube was introduced into the detection beam path, so that the reflected laser light could be guided to an optical bridge detector with a pair of balanced photodiodes (see [32] for details). The difference signal from the photodiodes was detected using a lock-in amplifier. MOKE loops were measured by tracking the difference sig-

nal as a function of the applied magnetic field controlled by the bipolar current source.

IV. ACKNOWLEDGEMENTS

The authors gratefully acknowledge technical assistance by E. Moldt and fruitful discussions with R. Edhib. S. D. acknowledges financial support by the Humboldt foundation and a startup funding grant provided by the DFG *via* SPP2244. The authors also acknowledge financial support by the DFG *via* the following grants: SFB1477 (project No. 441234705), SPP2244 (project No. 443361515) and KO3612/7-1 (project No. 467549803). K. W. and T. T. acknowledge support from the JSPS KAKENHI (grant numbers 20H00354 and 23H02052).

-
- [1] A. K. Geim and I. V. Grigorieva, *Nature* **499**, 419 (2013).
- [2] K. F. Mak, C. Lee, J. Hone, J. Shan, and T. F. Heinz, *Phys. Rev. Lett.* **105**, 136805 (2010).
- [3] D. Xiao, G. B. Liu, W. Feng, X. Xu, and W. Yao, *Phys. Rev. Lett.* **108**, 196802 (2012).
- [4] J. F. Sierra, J. Fabian, R. K. Kawakami, S. Roche, and S. O. Valenzuela, *Nature Nanotechnology* **16**, 856 (2021).
- [5] J. R. Schaibley, H. Yu, G. Clark, P. Rivera, J. S. Ross, K. L. Seyler, W. Yao, and X. Xu, *Nature Reviews Materials* **1**, 16055 (2016).
- [6] K. F. Mak, K. He, J. Shan, and T. F. Heinz, *Nat. Nano.* **7**, 494 (2012).
- [7] H. Zeng, J. Dai, W. Yao, D. Xiao, and X. Cui, *Nat. Nano.* **7**, 490 (2012).
- [8] G. Wang, E. Palleau, T. Amand, S. Tongay, X. Marie, and B. Urbaszek, *Applied Physics Letters* **106**, 112101 (2015).
- [9] M. Baranowski, A. Surrente, D. K. Maude, M. Ballotín, A. A. Mitioglu, P. C. M. Christianen, Y. C. Kung, D. Dumcenco, A. Kis, and P. Plochocka, *2D Materials* **4**, 025016 (2017).
- [10] H. Tornatzky, A.-M. Kaulitz, and J. Maultzsch, *Phys. Rev. Lett.* **121**, 167401 (2018).
- [11] D. MacNeill, C. Heikes, K. F. Mak, Z. Anderson, A. Kormányos, V. Zólyomi, J. Park, and D. C. Ralph, *Phys. Rev. Lett.* **114**, 037401 (2015).
- [12] A. Mitioglu, P. P. Plochocka-Maude, A. Granados del Aguila, P. C. M. Christianen, G. Deligeorgis, S. Anghel, L. Kulyuk, and D. K. Maude, *Nano Lett.* **15**, 150611125011005 (2015).
- [13] B. Scharf, G. Xu, A. Matos-Abiague, and I. Žutić, *Phys. Rev. Lett.* **119**, 127403 (2017).
- [14] D. Zhong, K. L. Seyler, X. Linpeng, R. Cheng, N. Sivadas, B. Huang, E. Schmidgall, T. Taniguchi, K. Watanabe, M. A. McGuire, W. Yao, D. Xiao, K.-M. C. Fu, and X. Xu, *Science Advances* **3**, e1603113 (2017).
- [15] Y. Ye, J. Xiao, H. Wang, Z. Ye, H. Zhu, M. Zhao, Y. Wang, J. Zhao, X. Yin, and X. Zhang, *Nature Nanotechnology* **11**, 598 (2016).
- [16] H. Tornatzky, C. Robert, P. Renucci, B. Han, T. Blon, B. Lassagne, G. Ballon, Y. Lu, K. Watanabe, T. Taniguchi, B. Urbaszek, J. M. J. Lopes, and X. Marie, *Applied Physics Letters* **119**, 263103 (2021).
- [17] C. Zhao, T. Norden, P. Zhang, P. Zhao, Y. Cheng, F. Sun, J. P. Parry, P. Taheri, J. Wang, Y. Yang, T. Scrace, K. Kang, S. Yang, G.-x. Miao, R. Sabirianov, G. Kioseoglou, W. Huang, A. Petrou, and H. Zeng, *Nature Nanotechnology* **12**, 757 (2017).
- [18] K. F. Mak, J. Shan, and D. C. Ralph, *Nature Reviews Physics* **1**, 646 (2019).
- [19] S. Zhang, H. Wu, L. Yang, G. Zhang, Y. Xie, L. Zhang, W. Zhang, and H. Chang, *Mater. Horiz.* **9**, 559 (2022).
- [20] T. P. Lyons, D. Gillard, A. Molina-Sánchez, A. Misra, F. Withers, P. S. Keatley, A. Kozikov, T. Taniguchi, K. Watanabe, K. S. Novoselov, J. Fernández-Rossier, and A. I. Tartakovskii, *Nature Communications* **11**, 6021 (2020).
- [21] S. Rahman, B. Liu, B. Wang, Y. Tang, and Y. Lu, *ACS Applied Materials & Interfaces* **13**, 7423 (2021).
- [22] T. Zhang, S. Zhao, A. Wang, Z. Xiong, Y. Liu, M. Xi, S. Li, H. Lei, Z. V. Han, and F. Wang, *Advanced Functional Materials* **32**, 2204779 (2022).
- [23] C. Gong, L. Li, Z. Li, H. Ji, A. Stern, Y. Xia, T. Cao, W. Bao, C. Wang, Y. Wang, Z. Q. Qiu, R. J. Cava, S. G. Louie, J. Xia, and X. Zhang, *Nature* **546**, 265 (2017).
- [24] Y. F. Li, W. Wang, W. Guo, C. Y. Gu, H. Y. Sun, L. He, J. Zhou, Z. B. Gu, Y. F. Nie, and X. Q. Pan, *Phys. Rev. B* **98**, 125127 (2018).
- [25] H. Fang, C. Battaglia, C. Carraro, S. Nemsak, B. Ozdol, J. S. Kang, H. A. Bechtel, S. B. Desai, F. Kronast, A. A. Unal, G. Conti, C. Conlon, G. K. Palsson, M. C. Martin, A. M. Minor, C. S. Fadley, E. Yablonovitch, R. Maboudian, and A. Javey, *Proceedings of the National Academy of Sciences* **111**, 6198 (2014).
- [26] A. Vervelaki, K. Bagani, D. Jetter, M.-H. Doan, T. K. Chau, B. Gross, D. V. Christensen, P. Bøggild, and M. Poggio, *Communications Materials* **5**, 10.1038/s43246-024-00477-5 (2024).
- [27] A. Noah, H. Alpern, S. Singh, A. Gutfreund, G. Zisman, T. D. Feld, A. Vakahi, S. Remennik, Y. Paltiel, M. E. Huber, V. Barrena, H. Suderow, H. Steinberg, O. Millo, and Y. Anahory, *Nano Letters* **22**, 3165 (2022).
- [28] C. Robert, D. Lagarde, F. Cadiz, G. Wang, B. Lassagne, T. Amand, A. Balocchi, P. Renucci, S. Tongay,

- B. Urbaszek, and X. Marie, *Phys. Rev. B* **93**, 205423 (2016).
- [29] M. M. Glazov, T. Amand, X. Marie, D. Lagarde, L. Bouet, and B. Urbaszek, *Physical Review B* **89**, 201302 (2014).
- [30] A. Castellanos-Gomez, M. Buscema, R. Molenaar, V. Singh, L. Janssen, H. S. J. van der Zant, and G. A. Steele, *2D Materials* **1**, 011002 (2014).
- [31] P. Gant, F. Carrascoso, Q. Zhao, Y. K. Ryu, M. Seitz, F. Prins, R. Frisenda, and A. Castellanos-Gomez, *2D Materials* **7**, 025034 (2020).
- [32] M. Kempf, A. Schubert, R. Schwartz, and T. Korn, *Review of Scientific Instruments* **92**, 113904 (2021).

V. SUPPLEMENT

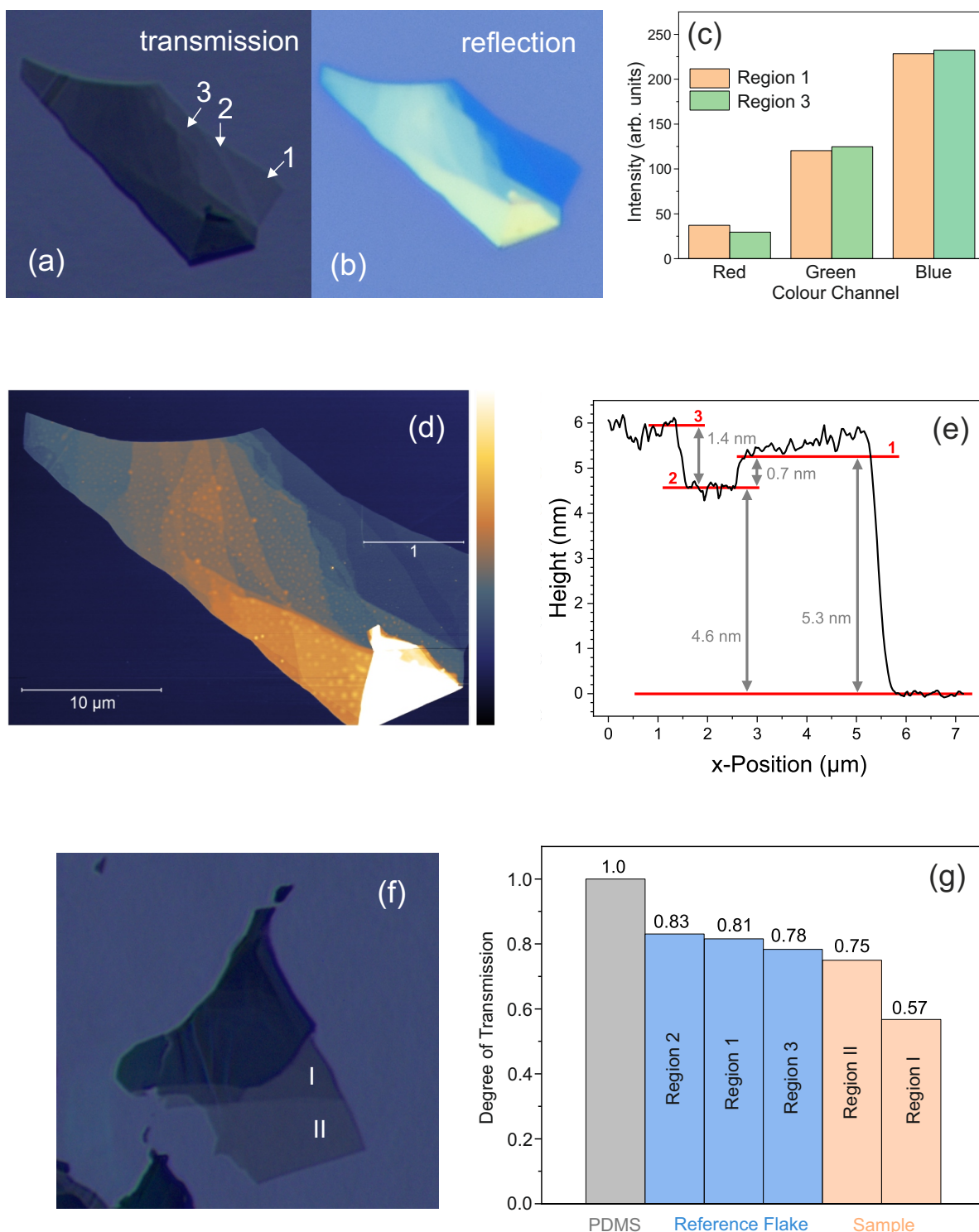


Figure 4. S1. The CGT sample thickness was determined using a reference sample. (a) The transmission microscopy image of the reference sample on PDMS shows three thin regions (1-3) of different thickness. Here, a clear contrast between 1 and 2 is visible, whereas the contrast between 1 and 3 is poor. The reflection light image (b) of the same sample on a Si/SiO₂ substrate reveals a difference in layer thickness between 1 and 3 which manifests itself in different nuances of blue. The contrast is reflected in all colour channels (c). (d,e) AFM measurements were performed to elucidate the actual sample thickness. Assuming a monolayer step height of 1.1 nm and a step height of 0.7 nm for every subsequent layer in accordance with [23], region 2 consists of 6, region 1 of 7 and region 3 of 8 layers. (f,g) From the transmission microscopy images the degree of transmission for the reference flake and the CGT flake shown in the main text was determined, using the PDMS film as a calibration. We assume a reduction of about 3 percent per layer. A comparison between the values for the flake shown in the main text and the reference flake hints at layer thicknesses of 9 layers in region I and 14 layers in region II.

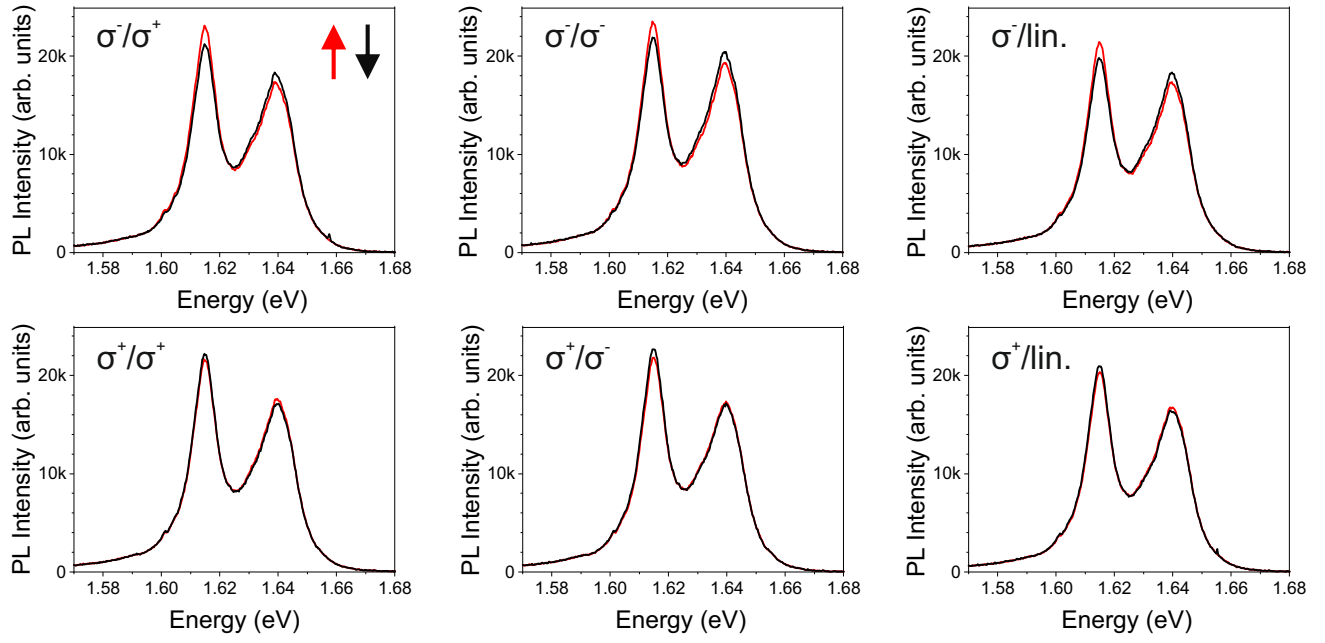


Figure 5. **S2.** PL spectra for different (excitation/detection) helicities and magnetic field directions (arrows). For a constant excitation helicity, the population dynamics is independent of the detection helicity.

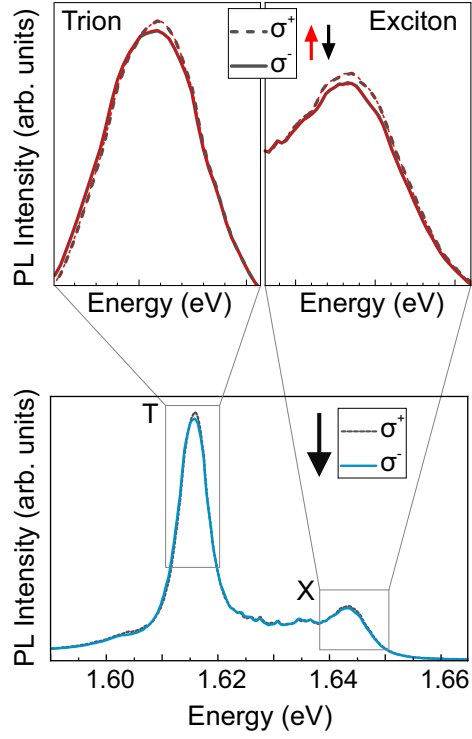


Figure 6. **S3.** No magnetic-field-dependent intensity differences for left (solid) and right (dashed line) circularly polarized excitation are detected in the isolated monolayer. This proves that the magnetic-field-dependent intensity differences result from an interaction between the MoSe₂ monolayer and the overlying CGT layer. For better visibility only the spectra for B_↓ are shown in the lower panel. The upper panels show a zoom in of trion and exciton peak for both magnetic field directions. Small intensity differences for left and right polarized excitation result from minor changes of laser excitation spot.